

Direct Visualization of the Reversible O²⁻/O⁻ Redox Process in Li-Rich Cathode Materials

Xiang Li, Yu Qiao, Shaohua Guo,* Zhenming Xu, Hong Zhu, Xiaoyu Zhang, Yang Yuan, Ping He,* Masayoshi Ishida, and Haoshen Zhou*

Conventional cathodes of Li-ion batteries mainly operate through an insertion–extraction process involving transition metal redox. These cathodes will not be able to meet the increasing requirements until lithium-rich layered oxides emerge with beyond-capacity performance. Nevertheless, in-depth understanding of the evolution of crystal and excess capacity delivered by Li-rich layered oxides is insufficient. Herein, various in situ technologies such as X-ray diffraction and Raman spectroscopy are employed for a typical material Li_{1.2}Ni_{0.2}Mn_{0.6}O₂, directly visualizing O⁻–O⁻ (peroxy oxygen dimers) bonding mostly along the *c*-axis and demonstrating the reversible O²⁻/O⁻ redox process. Additionally, the formation of the peroxy O–O bond is calculated via density functional theory, and the corresponding O–O bond length of ≈1.3 Å matches well with the in situ Raman results. These findings enrich the oxygen chemistry in layered oxides and open opportunities to design high-performance positive electrodes for lithium-ion batteries.

The applications of lithium-ion batteries (LIBs) like mobile devices are familiar in our daily lives.^[1] However, the energy density of nowadays LIBs is still unsatisfying toward our increasing requirements.^[2,3] The most common positive electrodes, such as LiCoO₂, LiFePO₄, and LiMn₂O₄, are still limited to the unsatisfied capacity, hindering the development of LIBs.^[4] To allay the gap between supply and demand, we should

settle the capacity issue. Therefore, aiming at improving the battery performance, a lot of efforts have been made in searching for better electrode materials with high capacity and good cyclic ability.^[5]

Recently, lithium-rich layered oxides like Li_{1.2}Ni_{0.166}Co_{0.067}Mn_{0.567}O₂ with higher capacities than 250 mA h g⁻¹ were reported.^[6] These Li-rich materials can deliver excess capacity beyond the theoretical capacity based on cationic redox process, having received worldwide attention. The compounds (1-x) LiNi_{0.5}Mn_{0.5}O₂·xLi₂MnO₃, which can be also written as Li[Li_{(1-2x)/3}Ni_xMn_{(2-x)/3}O₂], are well known.^[7,8] However, the mechanism based on cationic redox process is unable to explain the anomalous capacities exhibited by Li-rich materials. Thus,

another new process, oxygen activation has been proposed to account for the phenomenon. Luo et al. pointed out that localized electron holes are formed on oxygen ions with the configuration surrounding by Mn⁴⁺ and Li⁺ in Li_{1.2}[Ni_{0.13}Co_{0.13}Mn_{0.54}]O₂.^[9] Seo et al. depicted that oxygens are easily oxidized due to the Li–O–Li configuration.^[10] Sathiya et al. observed the peroxy-like species formed reversible in Li₂Ru_{1-y}Sn_yO₃.^[11] However, all above-mentioned results are lacking in direct especially in situ evidence for deep insight into the microstructure evolution of Li-rich layered oxides. McCalla et al. visualized the O–O dimers via transmission electron microscopy (TEM) and neutron powder diffraction by using Li₂IrO₃ as a model compound and determined the possible limits on the value of *n* for peroxy-like O₂ⁿ⁻ dimers (the lower bound *n* = 3 and the upper *n* = 3.3), leading to a further understanding of anionic redox process.^[12] Here, we focus on the representative material Li_{1.2}Ni_{0.2}Mn_{0.6}O₂ and investigate its charge–discharge processes during initial cycles by in situ X-ray diffraction (XRD) and in situ Raman spectroscopy. We demonstrate the structural change by the continuous shift of *c*-parameter and the direct evidence of peroxy O–O bond formation and extinction (O₂²⁻ dimers). What is more, the well reversible formation/extinction of the dimers can be clearly observed in subsequent cycles, accompanied with synchronous structural change. Moreover, we can speculate that the peroxy O–O bond is along the *c*-axis by combining the variation trend of *c* lattice and peroxy O–O bond distance. Our findings provide a direct and new evidence for the reversible anionic redox chemistry in Li-rich cathode materials and a guideline toward designing the next generation of cathode

X. Li, Prof. S. H. Guo, Dr. X. Y. Zhang, Y. Yuan, Prof. P. He, Prof. H. S. Zhou
Center of Energy Storage Materials and Technology

College of Engineering and Applied Sciences

National Laboratory of Solid State Microstructures, and Collaborative Innovation Center of Advanced Microstructure

Nanjing University

Nanjing 210093, China

E-mail: shguo@nju.edu.cn; pinghe@nju.edu.cn; hszhou@nju.edu.cn

X. Li, Y. Qiao, Prof. M. Ishida

Graduate School of System and Information Engineering

University of Tsukuba

Tennoudai 1-1, Tsukuba 305-8573, Japan

X. Li, Prof. S. H. Guo, Prof. H. S. Zhou

Energy Technology Research Institute

National Institute of Advanced Industrial Science and Technology (AIST)
Umezono 1-1-1, Tsukuba 305-8568, Japan

Z. Xu, Prof. H. Zhu

University of Michigan-Shanghai Jiao Tong University Joint Institute
Shanghai Jiao Tong University

Shanghai 200240, China

 The ORCID identification number(s) for the author(s) of this article can be found under <https://doi.org/10.1002/adma.201705197>.

DOI: 10.1002/adma.201705197

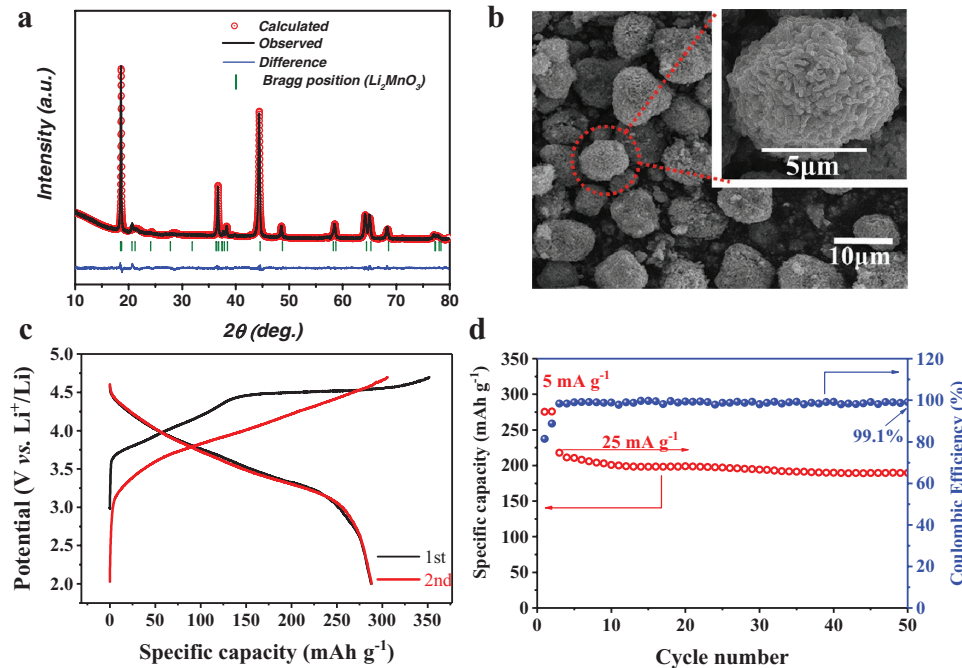


Figure 1. XRD, SEM, and electrochemical characterizations of $\text{Li}_{1.2}\text{Ni}_{0.2}\text{Mn}_{0.6}\text{O}_2$. a) XRD patterns of $\text{Li}_{1.2}\text{Ni}_{0.2}\text{Mn}_{0.6}\text{O}_2$ and Rietveld refinement. b) SEM images of $\text{Li}_{1.2}\text{Ni}_{0.2}\text{Mn}_{0.6}\text{O}_2$. The inset shows a zoom-in image of the particle marked by the red dotted line. c) Typical charge–discharge profiles between 2.0 and 4.7 V at 5 mA g^{-1} . d) The cycling performance with coulombic efficiency at 5 mA g^{-1} (first two cycles) and 25 mA g^{-1} (subsequent cycles).

materials with both cationic and anionic reversible redox process which can deliver substantially high energy density.

The compound was characterized by powder XRD and scanning electron microscopy (SEM) in Figure 1a,b. $\text{Li}_{1.2}\text{Ni}_{0.2}\text{Mn}_{0.6}\text{O}_2$ is derived from Li_2MnO_3 by using Ni^{2+} to replace partial Li^+ and Mn^{4+} in transition metal (TM) layers. The XRD pattern indicates that most of the diffraction lines can be well indexed to a monoclinic Li_2MnO_3 -like structure with space group $C2/m$.^[13] Rietveld refinements of the XRD pattern obtained by the General Structure Analysis System (GSAS) + EXPGUI suite^[14] successfully give reasonably low χ^2 (2.72) value based on Li_2MnO_3 model. The calculated XRD patterns have a good match with experimental data. The detailed refinement results are shown in Table S17 in the Supporting Information. SEM images in Figure 1b reveal that spheroidal particles with a diameter of around 8 μm are secondary particles formed from primary nanocrystals. The morphology of the particles is inherited from their hydroxide precursors (Figure S1, Supporting Information).

The electrochemical tests of as-prepared cathode were performed galvanostatically within the potential window (vs Li/Li^+) of 2.0–4.7 V using 5 mA g^{-1} . Figure 1c shows the results during the first two cycles and corresponding dQ/dV curves can be seen in Figure S2 in the Supporting Information. During the first charging process, the peaks located at ≈ 3.75 and 4.2 V are ascribed to the separate oxidation of nickel. The slope and plateau in initial charging process relate to the different Li^+ extraction processes. It is easy to see the capacity of first charging is 350 mA h g^{-1} , indicating there are more than 1.1 Li^+ removed from the structure. It is worth noting that there are only 0.4 Li^+ can be removed when Ni^{2+} is totally oxidized to Ni^{4+} , corresponding $\approx 130 \text{ mA h g}^{-1}$ at this point, far less than 350 .^[3,8,15] The capacity of first discharging is $\approx 287 \text{ mA h g}^{-1}$, indicating

that there are about 0.9 Li^+ reinserted into the structure, leading to about 0.2 Li^+ loss. Figure 1d presents the cycling performance and coulombic efficiency. The capacity retention of the cathode at 25 mA g^{-1} after 50 cycles is 90.90% with limited capacity decay. If we focus on cations in this composition, capacity will only come from Ni-based redox process because of electrochemical inertness of Mn^{4+} .^[4] As mentioned above, it is available to understand the relationship between the excess capacity and the evolution of the structure.

To unveil the lithiation–delithiation mechanism in $\text{Li}_{1.2}\text{Ni}_{0.2}\text{Mn}_{0.6}\text{O}_2$ during cycling processes, in situ XRD was performed for the initial two cycles, displayed in Figure 2 and Figure S4 in the Supporting Information. The XRD pattern of cathode material assembled in the in situ cell before test is shown in Figure S3 in the Supporting Information. For the reason of structural similarity between Li_2MnO_3 and $\text{LiNi}_{0.5}\text{Mn}_{0.5}\text{O}_2$, in situ XRD patterns can be fitted to hexagonal unit cell for convenience.^[16] As it can be seen, the peak position, such as (003) and (104), changes regularly with the process of charging and discharging, representing reversible Li-ion insertion–extraction during the test. (003) peak directly reflects the evolution of c lattice parameter of the compound. Therefore, it can be used for further understanding of the phase transformation mechanism in the system. As seen in Figure 2, at the beginning of the first charging, (003) peak shifts to the left continuously then gradually shifts back to the high angle region till the end of charging. The electrochemical record shows the turning point of (003) shifting is around 4.5 V. It means c lattice value increases at first until the voltage reaches to 4.5 V, followed by a sequential decrease. During discharging, reversed shift compared to the charging process is obvious. The evolution of (003) peak shifting within the first two cycles can

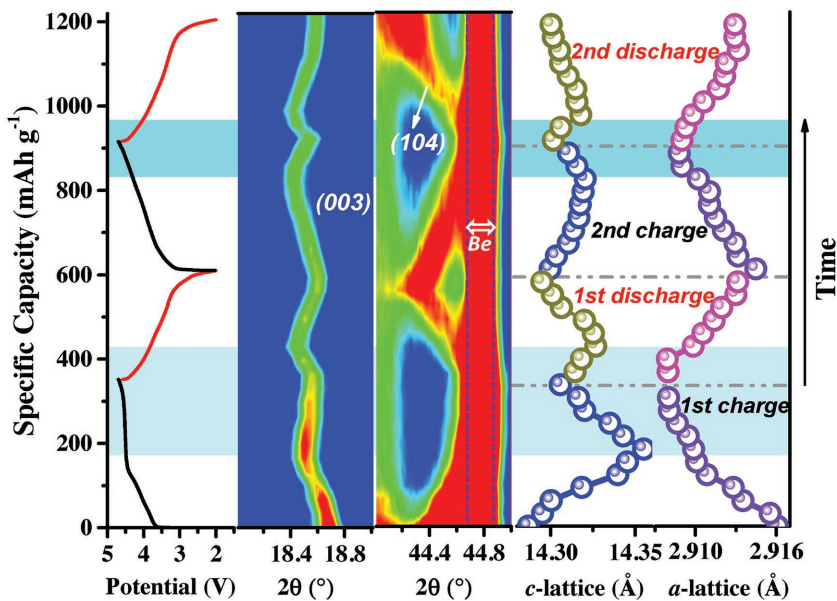


Figure 2. Color-coded images of the peak (003) and (104), refined *c*-lattice, and *a*-lattice parameters during initial two cycles. The range of intensity distribution plots with reference color bar is from 3000 to 5000.

be seen clearly in color graph in Figure 2. More importantly, this tendency of (003) shifts during the second cycle is similar to the first cycle.

The Rietveld refinement of the *a* and *c* lattice parameters for the structure together with corresponding unit cell volume changing during the first two cycles are displayed in Figure 2 and Figure S5 in the Supporting Information. Figure 2 discloses the *a*-lattice parameter continuously decrease whereas *c*-lattice parameter increases at the beginning and then decreases during the charge steps. At the beginning, the reduced ionic

radii in TM layers may be the reason why *a*-parameter decreases.^[4] The extraction of Li⁺ from the Li-layers is accompanied by the increasing electrostatic repulsion between oxygen slabs, making an extendibility of unit cell along *c*-axis, corresponding to the shift of (003) to lower angles.^[17] And then, the *c*-parameter and *a*-parameter change smoothly, indicating that some different reactions appear in this region. And during this region, Li⁺ begins to extract from the TM slabs, leading the inverse changes of unit cell and shifting (003) peak to higher reflection angles. The variation is consistent with the previous work.^[18] During discharge, the reversed shift of the (003), (104) peak can be observed, indicating some opposite processes happens compared with charging. Notably, the changes of the peaks' position during the 2nd cycle are analogous to the first cycle, representing the parallel lithiation-delithiation mechanism, which coincides with the discussion above.

Recently, the observation of higher capacity in relevant systems tends to be ascribed to the oxygen-related anionic electrochemical process.^[9,19,20] Thus, as a powerful tool to investigate the oxygen redox behaviors,^[21,22] *in situ* Raman has been employed (Figure 3, wider Raman shift region is shown in Figure S6, Supporting Information). In order to collect shell-isolated nanoparticle-enhanced Raman signal, gold nanoparticles (NPs) ≈40 nm in diameter with an SiO₂ coating shell (\approx 5 nm) were synthesized as in previous reports.^[23] The washed and dried Au@SiO₂ NPs were dripped onto the specific cathode surface and vacuum dried before assembly. Regardless of the

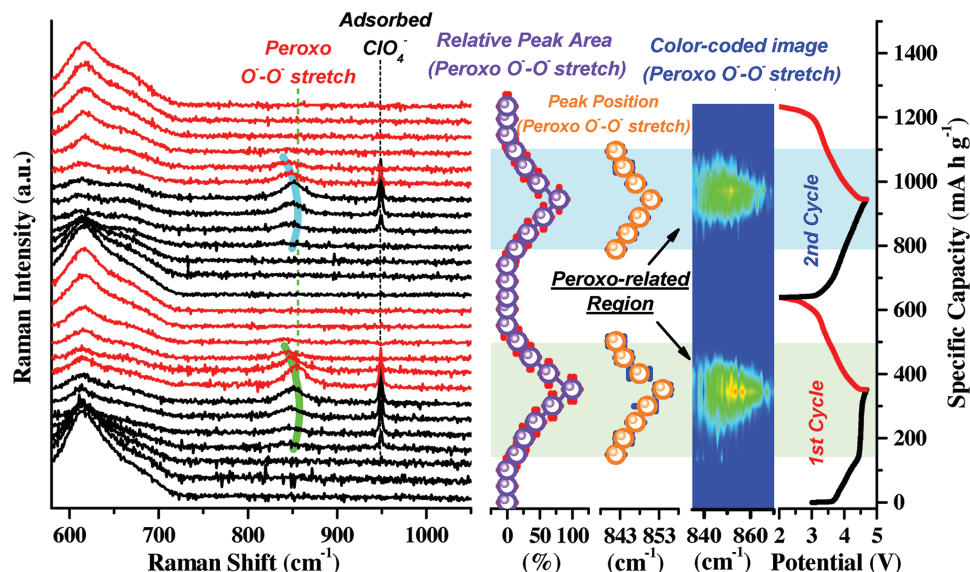


Figure 3. Capacity dependent *in situ* Raman spectra recorded during initial two galvanostatic cycles (5 mA g⁻¹). The novel peroxy-species peak has been highlighted, and corresponding capacity dependence of peak area (purple hollow), peak position (orange hollow), and color-coded image are summarized, respectively. The range of intensity distribution plots with reference color bar is from 0 to 0.03. The related voltage profiles are shown for clarity.

detailed analysis on overlapping stretching modes in MO_6 octahedron (below 700 cm^{-1}),^[24] the variation trend of several novel peaks become noteworthy during cycling. One sharp peak can be observed at 953 cm^{-1} once the potential climbs up to 4.4 V, which is due to the adsorption of the anion in perchlorate salt (ClO_4^- symmetric stretching).^[22] The related peak intensity quickly reaches maximum value due to the saturation of adsorption on the cathode surface. Besides, the unique adsorption feature can be further proved by the potential-dependent dropping trend during discharging (see more details in Figure S7, Supporting Information). More importantly, within the typical peroxy O–O stretch region (700–900 cm^{-1}) in peroxy-species (see more details in Figure S8, Supporting Information),^[9,22] a new peak at $\approx 850 \text{ cm}^{-1}$ emerges and increases during the 4.5 V related charging plateau, and gradually disappears with the subsequent discharge process. The potential of O–O peroxy bond appearance would be different in other systems resulting from different thermodynamic conditions, which means the environment (such as space group, neighbored atoms) surrounding oxygen atoms.^[25] The reversible variation trend of the peroxy O–O bond can also be obtained on specific high voltage plateau during the 2nd cycle. The average concentration of peroxy O–O bond can be represented by relative peak area which is also shown in Figure 3. The relative peak area of peroxy O–O bond equals zero (means no O–O bond appears) before 4.5 V related charging plateau, then increases gradually to the maximum corresponding to the end of charging as a function of time. The area decreases to zero subsequently in discharge process and exhibits reversible variation trend during the 2nd cycle. Moreover, according to the obtained XRD results (Figure 2), the formation of the newly proposed peroxy O–O bond can be assigned to the delithiation from Li/TM layer. During charging at 4.5 V plateau, the shift of peroxy O–O stretch to higher wavenumber indicates the reduction of peroxy O–O bond length in peroxy-species.^[18] The peroxy O–O bond length range can be empirically considered as 1.28–1.48 Å (1.28 Å in Li_2O_2 where peroxy O–O bond located at 790 cm^{-1} and 1.48 Å in H_2O_2 where peroxy O–O bond located at 878 cm^{-1}).^[26] Combining with the decreasing trend of *c*-axis length during related stage (Figure 2), the peroxy O–O bond tends to be formed along the *c*-axis (not in *ab* plane), which is also well consistent with the mechanism proposed by related density functional theory (DFT) simulations.^[27] In this case, the causality among delithiation/lithiation between Li/TM layer, the variation of *c*-axis and the formation/decomposition of peroxy O–O bond can be rationally unified together. Consequently, essentially different from the peroxy-like (O_2)ⁿ⁻-based redox process proposed by previous ex situ X-ray photoelectron spectroscopy (XPS) analysis,^[11,19,28] herein, the operando observation and assignment of real peroxy O–O bond in peroxy-species provides new evidence for the reversible anionic redox chemistry in Li-rich cathode materials. Furthermore, the similar phenomenon in LiPF_6 -salt electrolyte (1 M in propylene carbonate) can be seen in Figure S9 in the Supporting Information. Moreover, XPS etching experiment reveals that the peroxy O–O bond exists both in the surface and in the bulk (see more details in Figure S10, Supporting Information).

Besides the typical irreversible oxygen loss (such as the formation of O_2 , O_2^-) in the lithium rich materials,^[9,29] herein, we demonstrate a reversible oxygen behavior with the generation of O_2^{2-} dimers, which can be sustainable in the subsequent cycle. To better understand the formation of the peroxy O–O bond during cycling, the first-principles calculations for the $\text{Li}_{1.2-x}\text{Ni}_{0.2}\text{Mn}_{0.6}\text{O}_2$ systems have been performed. We note that the excess lithium ordering in the transition metal layer of $\text{Li}_{1.2}\text{Ni}_{0.2}\text{Mn}_{0.6}\text{O}_2$ is very complicated and a mixture of different types of local ordering.^[30] However, the $\text{Li}_{1.2}\text{Ni}_{0.2}\text{Mn}_{0.6}\text{O}_2$ with honeycomb ordering of excess lithium atoms experiences an energy barrier of 1.4 eV for the formation of peroxy bonds, compared to 0.6–1 eV of Li_2MnO_3 ,^[31] which is not realistic to occur during the room temperature cycling (see Figures S11–S13, Supporting Information, for detailed discussions). Here, we are especially interested in $\text{Li}_{1.2}\text{Ni}_{0.2}\text{Mn}_{0.6}\text{O}_2$ with local straight-type tripolymers (Figure S14, Supporting Information), where the formation of peroxy bonds experiences no energy barrier during charging.

Thus, the $\text{Li}_{1.2}\text{Ni}_{0.2}\text{Mn}_{0.6}\text{O}_2$ crystal structure with local straight-type was built using a $5 \times 2 \times 1$ supercell of the $\text{R}\bar{3}\text{m}$ LiMnO_2 with partial Mn atoms replaced by Ni and Li atoms, as shown in Figure S14 in the Supporting Information. First, the $\text{Li}_{1.2}\text{Ni}_{0.2}\text{Mn}_{0.6}\text{O}_2$ crystal structure was relaxed, and the optimized lattice parameters of $\text{Li}_{1.2}\text{Ni}_{0.2}\text{Mn}_{0.6}\text{O}_2$ unit cell are $a = 14.49$, $b = 5.81$, and $c = 14.26 \text{ \AA}$, respectively. Then, the crystal structures and atomic positions of the $\text{Li}_{1.2-x}\text{Ni}_{0.2}\text{Mn}_{0.6}\text{O}_2$ systems during the whole charging processes were relaxed, and the corresponding charge density distributions for $x = 0.6$, 0.7, 0.8, 0.9, 1.0, and 1.1 were shown in Figure 4. During the initial charging process (x from 0 to 0.6), some lithium atoms in lithium layers are preferentially divorced from the $\text{Li}_{1.2-x}\text{Ni}_{0.2}\text{Mn}_{0.6}\text{O}_2$ cathode. No peroxy O–O bond is observed during this initial charging period. When reaching the middle period (i.e., $x = 0.7$), some excess lithium atoms in the TM-layers begin to leave from $\text{Li}_{0.5}\text{Ni}_{0.2}\text{Mn}_{0.6}\text{O}_2$ cathode, and two adjacent O atoms of the MnO_6 octahedron near the excess lithium vacancies get closer to each other. Moreover, remarkable electrons between these two closer O atoms can be observed (yellow isosurfaces in black dashed circles), demonstrating the formation of O–O covalent bond, and the corresponding O–O bond length is calculated to be 1.343 Å (Table 1), which is much shorter than 2.6 Å of interatomic distance between adjacent O atoms in MnO_6 octahedrons, and even shorter than 1.49 Å of the peroxy O–O bond length in Li-Rich Li_2MnO_3 system.^[31] According to the Bader charge data (Figure S15, Supporting Information), the O atomic charges of the special O–O bond in $\text{Li}_{0.5}\text{Ni}_{0.2}\text{Mn}_{0.6}\text{O}_2$ cathode are larger than those in $\text{Li}_{0.6}\text{Ni}_{0.2}\text{Mn}_{0.6}\text{O}_2$ and other O atoms far from the excess lithium vacancies. All these evidence indicate the formation of the peroxy O–O bond between $x = 0.6$ and 0.7, corresponding to the specific capacity between 190 and 220 mA h g⁻¹, which is consistent with the in situ Raman spectra data. During the final charging period ($x = 0.8$ –1.1), more and more peroxy O–O bonds form with smaller bond lengths and more positive O atomic charges, which is also consistent with the variation trend of Raman shift and relative peak area of O–O bonds in our in situ Raman spectra data.

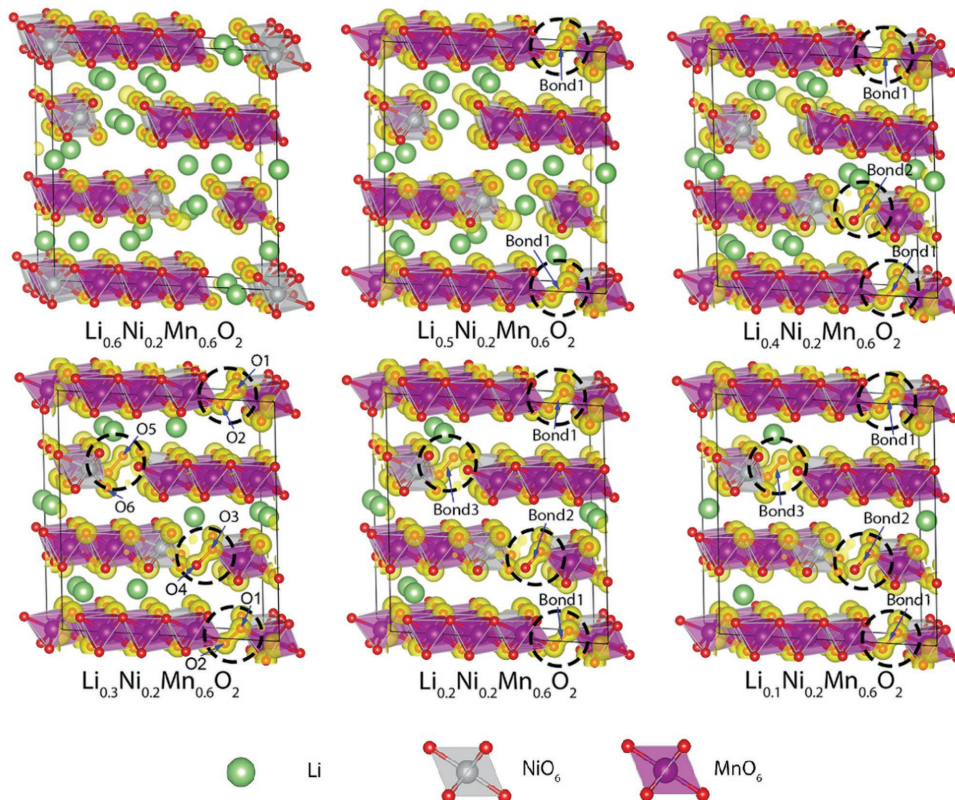


Figure 4. Charge density distributions (yellow isosurfaces = $0.2 \text{ e } \text{\AA}^{-3}$) of the $\text{Li}_{1.2-x}\text{Ni}_{0.2}\text{Mn}_{0.6}\text{O}_2$ systems ($x = 0.6, 0.7, 0.8, 0.9, 1.0$, and 1.1) with peroxy O–O bonds (in the black dashed circles) during the charging and discharging processes.

The processes summarizing the aforementioned discussion are as follows: At first, Li^+ migrates out from Li layers with the charge compensation by $\text{Ni}^{2+/4+}$ redox couple, corresponding to $\approx 130 \text{ mA h g}^{-1}$. From then on, oxidation of oxygen starts to emerge for charging compensation till the end of the charging because Ni^{2+} is totally oxidized to Ni^{4+} and Mn^{4+} cannot be oxidized to a higher valence state in octahedral site.^[32] Afterward, the oxidation of oxygen is the main responsible for charge compensation at the plateau of $\approx 4.5 \text{ V}$. Since about 1.1 Li^+ can be extracted from the structure, Li^+ continues to be removed out from Li layers and TM layers accompanied with appearance of peroxy O–O bond. The cooperative effect of anionic redox and extraction of Li^+ leads to the smooth change of c -lattice parameter and eventually turns it back to a lower value at this process. Figure S16 in the Supporting Information shows the par-

ticipation of Ni^{2+} and oxygen involvement during the charging process. The charge compensation during discharging process is similar with charging process. The changes of c -lattice parameter shows a cooperation including the reversible anionic (O^-/O^{2-}) redox process, the reduction of Ni and the reinsertion of Li^+ into the structure. Moreover, combining the changes of peroxy O–O bond length in Raman results with the variation tendency of c -axis length in XRD results, the formation of peroxy O–O bond is speculated along the c -axis, which is also confirmed by the DFT calculations.

In summary, the typical Li-rich positive material $\text{Li}_{1.2}\text{Ni}_{0.2}\text{Mn}_{0.6}\text{O}_2$ was systematically studied. Based on the advanced in situ technologies, we can directly visualize the structural evolution accompanied by the (de)lithiation, including the reversible anionic redox process, even peroxy O–O bond formation and extinction along c axis, which are consistent well with the DFT calculations. What is more, both cationic and anionic redox processes are reversible even in subsequent cycles, enabling Li-rich layered oxides a high capacity. Our findings highlight a new evidence for the reversible anionic redox process in Li-rich cathode materials and provide a deep understanding of intercalation chemistry and new insights into the design of high-performance Li-rich layered oxides.

Supporting Information

Supporting Information is available from the Wiley Online Library or from the author.

Acknowledgements

X.L. and Y.Q. contributed equally to this work. X.L. is grateful for financial support of the CSC (China Scholarship Council) scholarship. This work was partially supported financially by National Basic Research Program of China (2014CB932302 and 2014CB932303), Natural Science Foundation of Jiangsu Province of China (BK20170630), the Fundamental Research Funds for the Central Universities (021314380076 and 021314380080), the National Natural Science Foundation of China (21673116, 2163303, 51602144), and the Natural Science Foundation of Jiangsu Province of China (BK20160068). The authors are very grateful to Prof. Ying Shirley Meng and Prof. Shou-Hang Bo for the discussion.

Conflict of Interest

The authors declare no conflict of interest.

Keywords

in situ Raman spectroscopy, in situ X-ray diffraction, Li-ion batteries, Li-rich materials, oxygen redox

Received: September 11, 2017

Revised: January 5, 2018

Published online:

- [1] a) J. B. Goodenough, Y. Kim, *Chem. Mater.* **2010**, *22*, 587; b) M. S. Whittingham, *Chem. Rev.* **2004**, *104*, 4271; c) A. S. Arico, P. Bruce, B. Scrosati, J. M. Tarascon, W. Van Schalkwijk, *Nat. Mater.* **2005**, *4*, 366; d) J. M. Tarascon, M. Armand, *Nature* **2001**, *414*, 359; e) P. He, H. J. Yu, D. Li, H. S. Zhou, *J. Mater. Chem.* **2012**, *22*, 3680.
- [2] a) Z. D. Huang, X. M. Liu, B. A. Zhang, S. W. Oh, P. C. Ma, J. K. Kim, *Scr. Mater.* **2011**, *64*, 122; b) Y. Jiang, H. Zhuang, Q. L. Ma, Z. Jiao, H. J. Zhang, R. Z. Liu, Y. L. Chu, B. Zhao, *J. Mater. Res.* **2013**, *28*, 1505; c) S. Y. Yang, X. Y. Wang, X. K. Yang, L. Liu, Z. L. Liu, Y. S. Bai, Y. P. Wang, *J. Solid State Electrochem.* **2012**, *16*, 1229; d) L. J. Xi, C. W. Cao, R. G. Ma, Y. Wang, S. L. Yang, J. Q. Deng, M. Gao, F. Lian, Z. G. Lu, C. Y. Chung, *Phys. Chem. Chem. Phys.* **2013**, *15*, 16579.
- [3] J. S. Kim, C. S. Johnson, J. T. Vaughey, M. M. Thackeray, S. A. Hackney, *Chem. Mater.* **2004**, *16*, 1996.
- [4] D. L. Ye, G. Zeng, K. Nogita, K. Ozawa, M. Hankel, D. J. Searles, L. Z. Wang, *Adv. Funct. Mater.* **2015**, *25*, 7488.
- [5] Y. D. Wang, J. W. Jiang, J. R. Dahn, *Electrochim. Commun.* **2007**, *9*, 2534.
- [6] H. J. Yu, Y. G. So, A. Kuwabara, E. Tochigi, N. Shibata, T. Kudo, H. S. Zhou, Y. Ikuhara, *Nano Lett.* **2016**, *16*, 2907.
- [7] a) M. M. Thackeray, C. S. Johnson, J. T. Vaughey, N. Li, S. A. Hackney, *J. Mater. Chem.* **2005**, *15*, 2257; b) Z. H. Lu, D. D. MacNeil, J. R. Dahn, *Electrochim. Solid-State Lett.* **2001**, *4*, A191.
- [8] C. S. Johnson, J. S. Kim, C. Lefief, N. Li, J. T. Vaughey, M. M. Thackeray, *Electrochim. Commun.* **2004**, *6*, 1085.
- [9] K. Luo, M. R. Roberts, R. Hao, N. Guerrini, D. M. Pickup, Y. S. Liu, K. Edstrom, J. H. Guo, A. V. Chadwick, L. C. Duda, P. G. Bruce, *Nat. Chem.* **2016**, *8*, 684.
- [10] D. H. Seo, J. Lee, A. Urban, R. Malik, S. Kang, G. Ceder, *Nat. Chem.* **2016**, *8*, 692.
- [11] M. Sathiya, G. Rousse, K. Ramesha, C. P. Laisa, H. Vezin, M. T. Sougrati, M. L. Doublet, D. Foix, D. Gonbeau, W. Walker, A. S. Prakash, M. Ben Hassine, L. Dupont, J. M. Tarascon, *Nat. Mater.* **2013**, *12*, 827.
- [12] E. McCalla, A. M. Abakumov, M. Saubanere, D. Foix, E. J. Berg, G. Rousse, M. L. Doublet, D. Gonbeau, P. Novak, G. Van Tendeloo, R. Dominko, J. M. Tarascon, *Science* **2015**, *350*, 1516.
- [13] K. A. Jarvis, Z. Q. Deng, L. F. Allard, A. Manthiram, P. J. Ferreira, *Chem. Mater.* **2011**, *23*, 3614.
- [14] a) A. C. Larson, R. B. Von Dreele, *Los Alamos Natl. Lab. Rep.* **1994**, 86; b) B. H. Toby, *J. Appl. Crystallogr.* **2001**, *34*, 210.
- [15] Z. H. Lu, J. R. Dahn, *J. Electrochem. Soc.* **2002**, *149*, A1454.
- [16] a) L. Zhang, H. Noguchi, *J. Electrochem. Soc.* **2003**, *150*, A601; b) Z. H. Lu, L. Y. Beaulieu, R. A. Donaberger, C. L. Thomas, J. R. Dahn, *J. Electrochem. Soc.* **2002**, *149*, A778.
- [17] D. Mohanty, S. Kalnaus, R. A. Meisner, K. J. Rhodes, J. L. Li, E. A. Payzant, D. L. Wood, C. Daniel, *J. Power Sources* **2013**, *229*, 239.
- [18] J. M. Tarascon, G. Vaughan, Y. Chabre, L. Seguin, M. Anne, P. Strobel, G. Amatucci, *J. Solid State Chem.* **1999**, *147*, 410.
- [19] P. E. Pearce, A. J. Perez, G. Rousse, M. Saubanere, D. Batuk, D. Foix, E. McCalla, A. M. Abakumov, G. Van Tendeloo, M. L. Doublet, J. M. Tarascon, *Nat. Mater.* **2017**, *16*, 850.
- [20] B. Qiu, M. H. Zhang, Y. G. Xia, Z. P. Liu, Y. S. Meng, *Chem. Mater.* **2017**, *29*, 908.
- [21] Y. Qiao, S. Wu, J. Yi, Y. Sun, S. Guo, S. Yang, P. He, H. Zhou, *Angew. Chem., Int. Ed.* **2017**, *56*, 4960.
- [22] Y. Qiao, S. Ye, *J. Phys. Chem. C* **2015**, *119*, 12236.
- [23] J. F. Li, Y. F. Huang, Y. Ding, Z. L. Yang, S. B. Li, X. S. Zhou, F. R. Fan, W. Zhang, Z. Y. Zhou, D. Y. Wu, B. Ren, Z. L. Wang, Z. Q. Tian, *Nature* **2010**, *464*, 392.
- [24] P. Lanz, C. Villevieille, P. Novak, *Electrochim. Acta* **2014**, *130*, 206.
- [25] a) M. Sathiya, A. M. Abakumov, D. Foix, G. Rousse, K. Ramesha, M. Saubanere, M. L. Doublet, H. Vezin, C. P. Laisa, A. S. Prakash, D. Gonbeau, G. VanTendeloo, J. M. Tarascon, *Nat. Mater.* **2015**, *14*, 230; b) T. Ohzuku, A. Ueda, M. Nagayama, *J. Electrochem. Soc.* **1993**, *140*, 1862; c) S. H. Park, S. W. Oh, S. H. Kang, I. Belharouak, K. Amine, Y. K. Sun, *Electrochim. Acta* **2007**, *52*, 7226; d) N. Yabuuchi, K. Kubota, M. Dahbi, S. Kornaba, *Chem. Rev.* **2014**, *114*, 11636; e) M. Guignard, C. Didier, J. Darriet, P. Bordet, E. Elkäim, C. Delmas, *Nat. Mater.* **2013**, *12*, 74.
- [26] a) A. J. Bridgeman, J. Rothery, *J. Chem. Soc. Dalton Trans.* **1999**, 4077; b) Z. X. Liu, L. R. De Jesus, S. Banerjee, P. P. Mukherjee, *ACS Appl. Mater. Interfaces* **2016**, *8*, 23028.
- [27] M. Saubanere, E. McCalla, J. M. Tarascon, M. L. Doublet, *Energy Environ. Sci.* **2016**, *9*, 984.
- [28] D. Foix, M. Sathiya, E. McCalla, J. M. Tarascon, D. Gonbeau, *J. Phys. Chem. C* **2016**, *120*, 862.
- [29] a) A. R. Armstrong, M. Holzapfel, P. Novak, C. S. Johnson, S. H. Kang, M. M. Thackeray, P. G. Bruce, *J. Am. Chem. Soc.* **2006**, *128*, 8694; b) S. Hy, F. Felix, J. Rick, W. N. Su, B. J. Hwang, *J. Am. Chem. Soc.* **2014**, *136*, 999.
- [30] a) K. Luo, M. R. Roberts, N. Guerrini, N. Tapia-Ruiz, R. Hao, F. Massel, D. M. Pickup, S. Ramos, Y. S. Liu, J. Guo, *J. Am. Chem. Soc.* **2016**, *138*, 11211; b) M. Gu, I. Belharouak, A. Genc, Z. Wang, D. Wang, K. Amine, F. Gao, G. Zhou, S. Thevuthasan, D. R. Baer, *Nano Lett.* **2012**, *12*, 5186; c) M. M. Thackeray, S. H. Kang, C. S. Johnson, J. T. Vaughey, R. Benedek, S. Hackney, *J. Mater. Chem.* **2007**, *17*, 3112.
- [31] H. R. Chen, M. S. Islam, *Chem. Mater.* **2016**, *28*, 6656.
- [32] J. Roos, C. Eames, S. M. Wood, A. Whiteside, M. S. Islam, *Phys. Chem. Chem. Phys.* **2015**, *17*, 22259.

Copyright WILEY-VCH Verlag GmbH & Co. KGaA, 69469 Weinheim, Germany, 2018.

ADVANCED MATERIALS

Supporting Information

for *Adv. Mater.*, DOI: 10.1002/adma.201705197

Direct Visualization of the Reversible O²⁻/O⁻ Redox Process in Li-Rich Cathode Materials

Xiang Li, Yu Qiao, Shaohua Guo, Zhenming Xu, Hong Zhu,
Xiaoyu Zhang, Yang Yuan, Ping He,* Masayoshi Ishida, and
Haoshen Zhou**

Copyright WILEY-VCH Verlag GmbH & Co. KGaA, 69469 Weinheim, Germany, 2018.

Supporting Information

Direct Visualization of Reversible O²⁻/O⁻ Redox Process in Li-Rich Cathode Materials

Xiang Li, Yu Qiao, Shaohua Guo,* Zhenming Xu, Hong Zhu, Xiaoyu Zhang, Yang Yuan, Ping He,* Masayoshi Ishida, and Haoshen Zhou*

Experimental Section

Synthesis of Li_{1.2}Ni_{0.2}Mn_{0.6}O₂:

Co-precipitation method was used to prepare the precursor which can be found in our previous study.^[1] Reagents included ammonium hydroxide (AR, Nanjing Chemical Reagent Co., Ltd.), nickel sulfate hexahydrate (AR, Enox), manganese sulfate monohydrate (AR, Xilong Chemical Industry Co., Ltd.), and sodium hydroxide (AR, Nanjing Chemical Reagent Co., Ltd.). Briefly, the deoxidized aqueous solution of metal sulfates were slowly dropped into 1M NH₃(aq) controlled by peristaltic pumps, with stable PH value maintained by NaOH(aq). After filtering and washing adequately, the black precursor was dried in a drying oven at 80 °C for 10 h.

As-prepared precursor Ni_xMn_yOH (x:y=1:3) was mixed with 3 wt% excess LiOH·H₂O powders thoroughly, then, Li_{1.2}Ni_{0.2}Mn_{0.6}O₂ was obtained by calcining the mixture in the furnace at 750 °C for 12 h in air.

Characterizations:

The structure of Li_{1.2}Ni_{0.2}Mn_{0.6}O₂ was identified by powder XRD (Ultima III, Rigaku Corporation) radiation from Cu K α ($\lambda = 1.5406 \text{ \AA}$). The data were collected between diffraction angles (2θ) from 10° to 80° at a scan rate of 2° per min. Rietveld refinements of the XRD pattern obtained by GSAS + EXPGUI suite. The morphologies of the materials were procured by SEM (JSM-7000F). In-situ Raman spectra of the materials were obtained using a homemade mould and JASCO microscope spectrometer (NRS-1000DT).

Electrochemical tests:

2032 coin-type cells were used for electrochemical measurements. The electrodes consisted of active material, acetylene black, and polytetrafluoroethylene (PTFE, 12 wt.%) binder with the weight ratio of 85:10:5. 1 M LiClO₄ in propylene carbonate (PC) was prepared as the electrolyte. LAND 2001A Battery Testing Systems (Wuhan LAND electronics Co., Ltd, P.R. China) were employed for galvanostatic testing.

In-situ Raman observation:

A detailed description of the modified in-situ Raman cell (Hohsen Corp., Osaka, Japan) for the Li-ion battery employed in this study can be found in our previous study.^[2] In detail, a thin quartz window (thickness, 0.5 mm) has been fixed on the top of the cell as a sight window. In order to collect shell-isolated nanoparticle-enhanced Raman (SHINER) signal, gold nanoparticles (NPs) approximately 40 nm in diameter with a SiO₂ coating shell (~5 nm) were synthesized as in previous reports.^[3] The washed and dried Au@SiO₂ NPs were dripped onto the specific cathode surface and vacuum dried before assembly. The cathode was assembled at the bottom of the cell with the active material-face upward. On the top of the cathode, 50–100 μL of electrolyte was homogeneously dropped onto the glassy fiber filter separator (GF/A, Whatman). As a standard two-electrode configuration cell, lithium foil (thickness, 0.4 mm) was assembled at the top as the reference and counter electrode. Note that, a small hole was punched on the center of both the separator and Li foil, through which the laser and Raman signals can fluidly cross. The cell was assembled in an argon-filled glovebox.

The Raman spectra were recorded using a JASCO microscope spectrometer (NRS-1000DT). The excitation light of an air-cooled He–Ne laser at 632.8 nm wavelength was focused on the electrode surface through a 50×long working distance lens (Olympus America Inc.). The confocal slit was adjusted to be 4.0 μm to minimize the band broadening effect due to the contribution of non-confocal signal. The scattered light was collected in a backscattering geometry along the same optical path as the pumping laser. The power of laser beam delivered to the electrode surface was roughly 10% of the maximum 30 mW laser intensity, unless specified, to avoid degradation to the products and/or cathode. The Raman spectrum acquisition time varied from 600~800 s with 2 accumulations. At least 3 different places on the electrode surface at each cathode plate were checked to ensure the Raman spectra were credible and reproducible. The spectral resolution of the Raman spectra in the study was ca. 1.0 cm⁻¹.

For the in-situ Raman test, the electrochemical experiments were carried out under the control of a potentiostat (Potentiostat/Galvanostat PGSTAT30, Autolab Co. Ltd., Netherlands) at room temperature. The current and potential outputs from the potentiostat were recorded by a multifunction data acquisition module/amplifier (PGSTAT30 Differential Electrometer, Autolab), which was controlled by General Purpose Electrochemical Software (GPES). Typically, the galvanostatic control was carried out at a current density of 5 mA g⁻¹. Before characterization, the cell was kept on an open circuit for 10 h. The OCP was approximately 3.0 V in most cases in the study. All of the potentials in this study were referenced to Li/Li⁺.

DFT Calculation:

All calculations were carried out by using the projector augmented wave (PAW) method^[4] in the framework of DFT^[5], as implemented in the Vienna *ab-initio* Simulation Package (VASP). The generalized gradient approximation (GGA)^[6] and Perdew–Burke–Ernzerhof (PBE) exchange functional^[5] was used. The periodic boundary condition approach was used. The plane-wave energy cutoff was set to 450 eV. The Monkhorst–Pack method^[7] with 1×4×1 *k*-points mesh was employed for the Brillouin zone sampling of the structural relaxations of Li_{1.2-x}Ni_{0.2}Mn_{0.6}O₂. The convergence criterions of the energy and force were 10⁻⁴ eV/atom and 0.05 eV Å⁻¹, respectively.

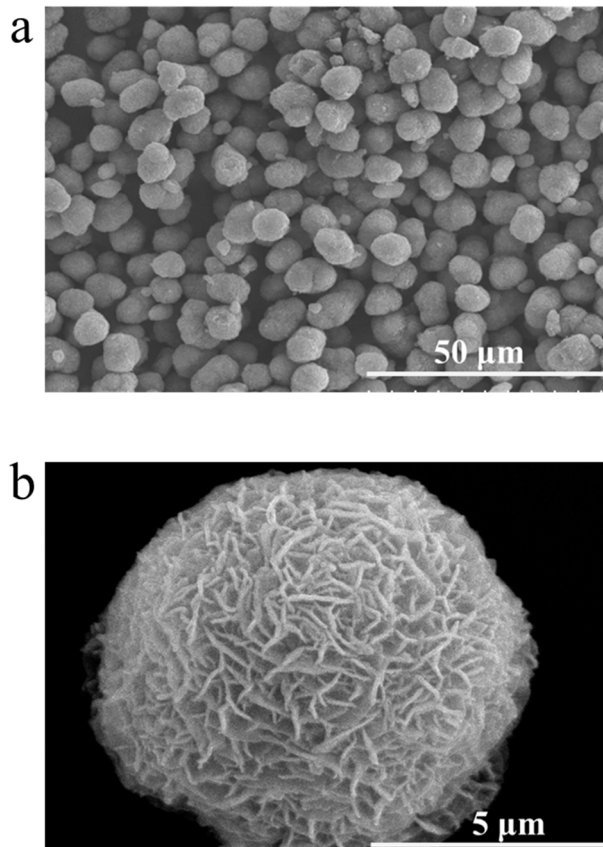


Figure S1. SEM images of precursor in different magnification. $\times 1.0\text{ k}$ (a) and $\times 10.0\text{ k}$ (b).

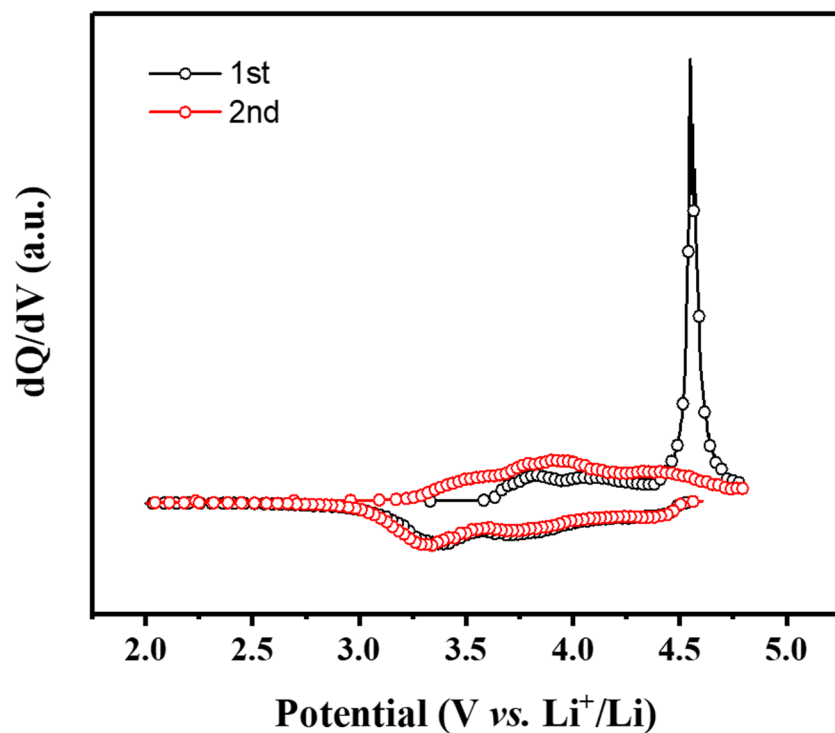


Figure S2. dQ/dV curves for initial two cycles of $\text{Li}_{1.2}\text{Ni}_{0.2}\text{Mn}_{0.6}\text{O}_2$ at 5 mA g^{-1} . The black dotted line represents the first cycle and the red dotted line represents the second cycle.

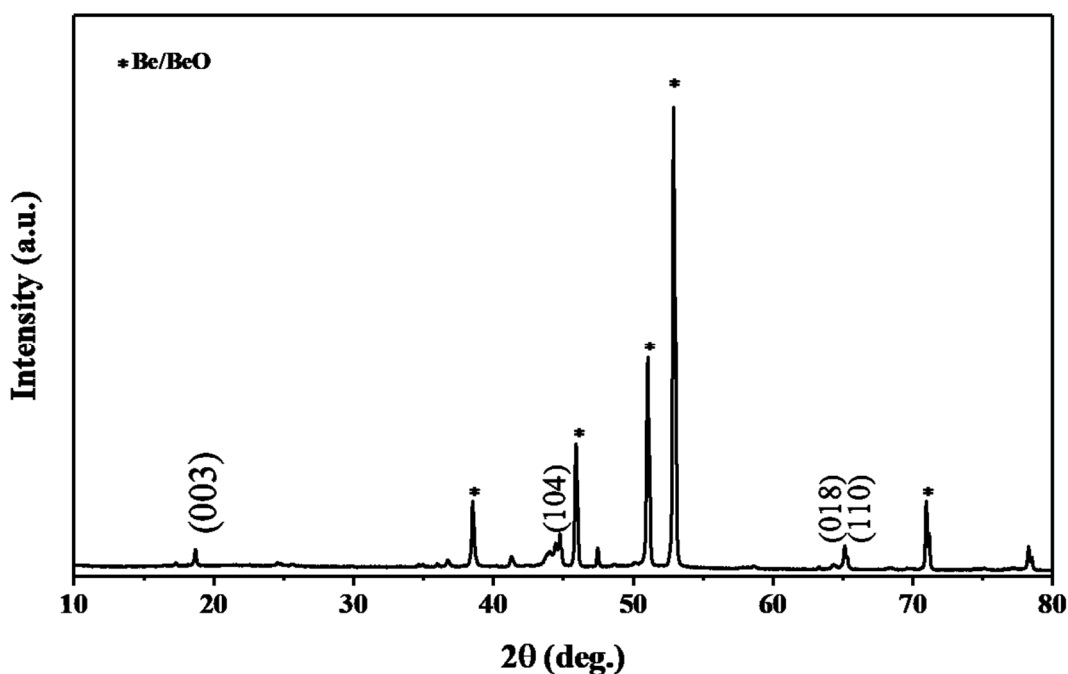


Figure S3. XRD pattern of $\text{Li}_{1.2}\text{Ni}_{0.2}\text{Mn}_{0.6}\text{O}_2$ in the in-situ mold. Peaks marked by * belong to Be/BeO.

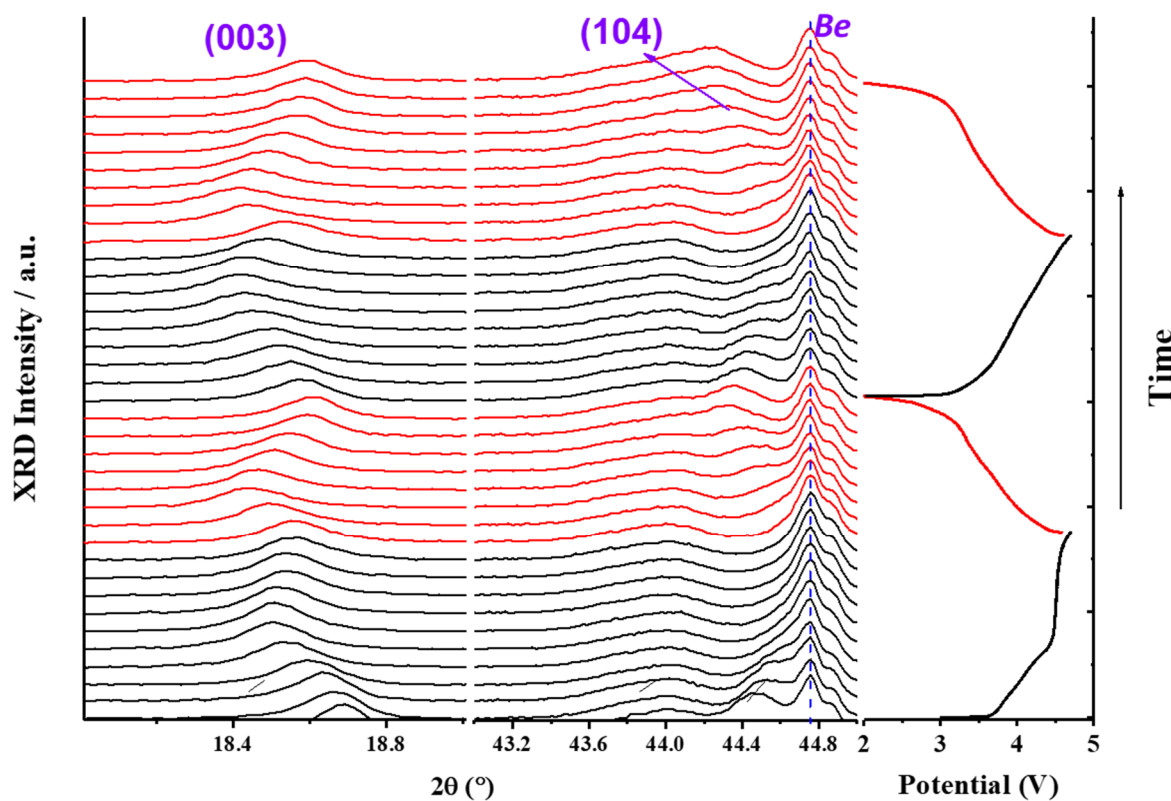


Figure S4. The in-situ XRD patterns of the evolution for the peaks (003) and (104), combined with corresponding electrochemical testing result during the first two cycles for the material $\text{Li}_{1.2}\text{Ni}_{0.2}\text{Mn}_{0.6}\text{O}_2$. The black line represents the charge process and the red line represents the discharge process.

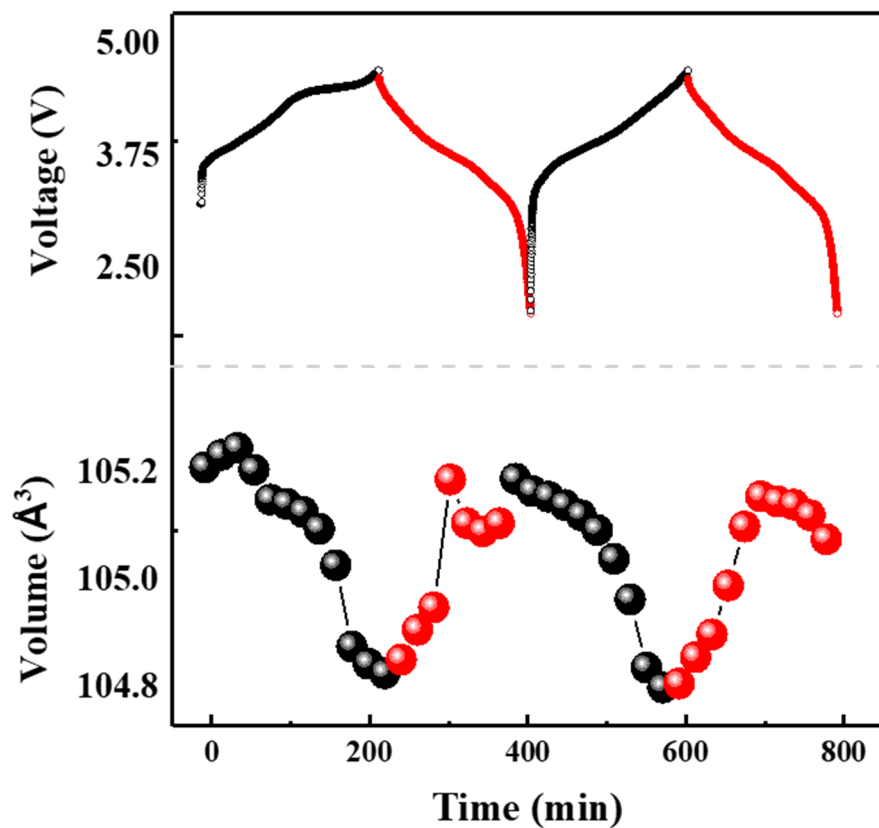


Figure S5. The charging and discharging curves of the first two cycles and changes of the Rietveld refined unit cell volume for $\text{Li}_{1.2}\text{Ni}_{0.2}\text{Mn}_{0.6}\text{O}_2$. The black and red colors represent charging and discharging process respectively.

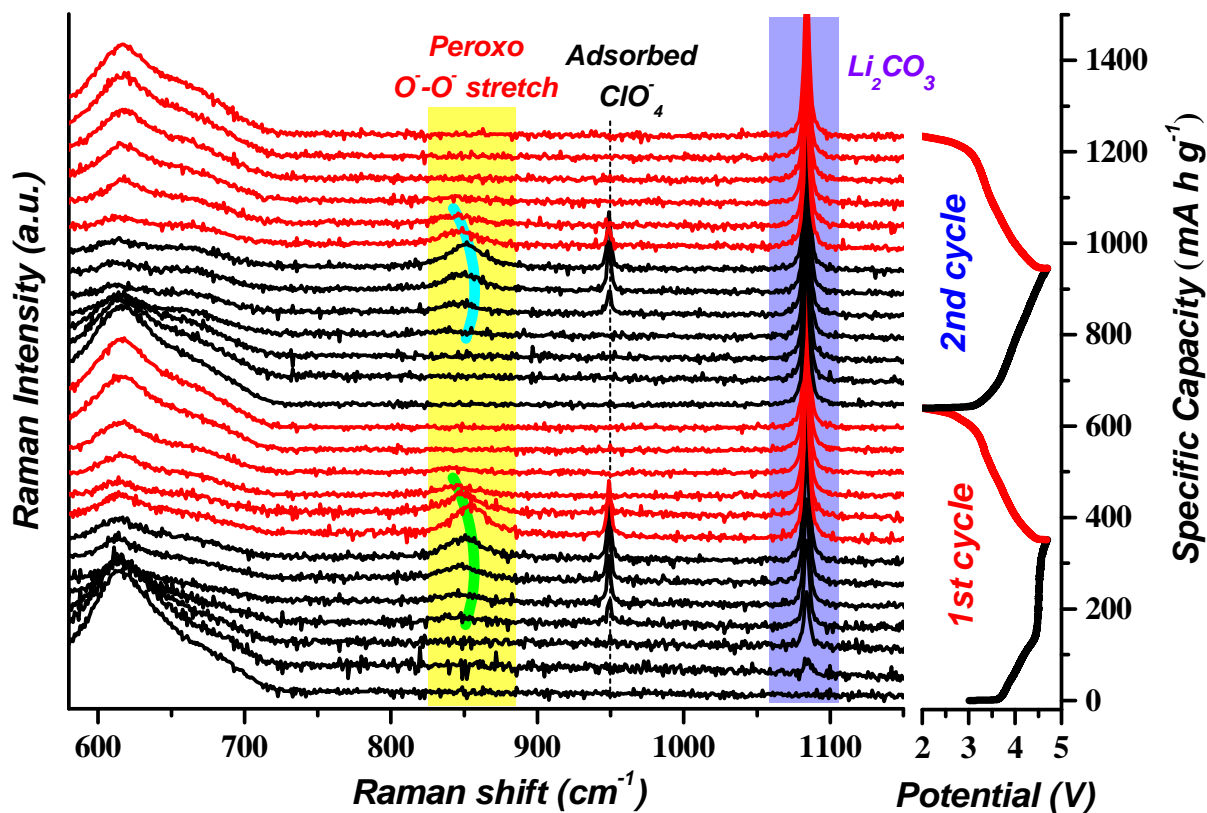


Figure S6. In situ Raman spectra (SERS-signal) recorded during initial two galvanostatic cycles with extended Raman shift range, which includes Li_2CO_3 -related peak ($\sim 1080 \text{ cm}^{-1}$) as comparison. Note that, the formation of carbonate species would be rationally ascribed to the parasitic reaction between electrolyte and other active oxygen-related species (superoxide anion radical and/or oxygen), which release from the lattice ($\text{Li}_{1.2}\text{Ni}_{0.2}\text{Mn}_{0.6}\text{O}_2$) upon charging (irreversible oxygen loss). This parasitic accumulation of Li_2CO_3 is also well coincide with previous reports.^[8]

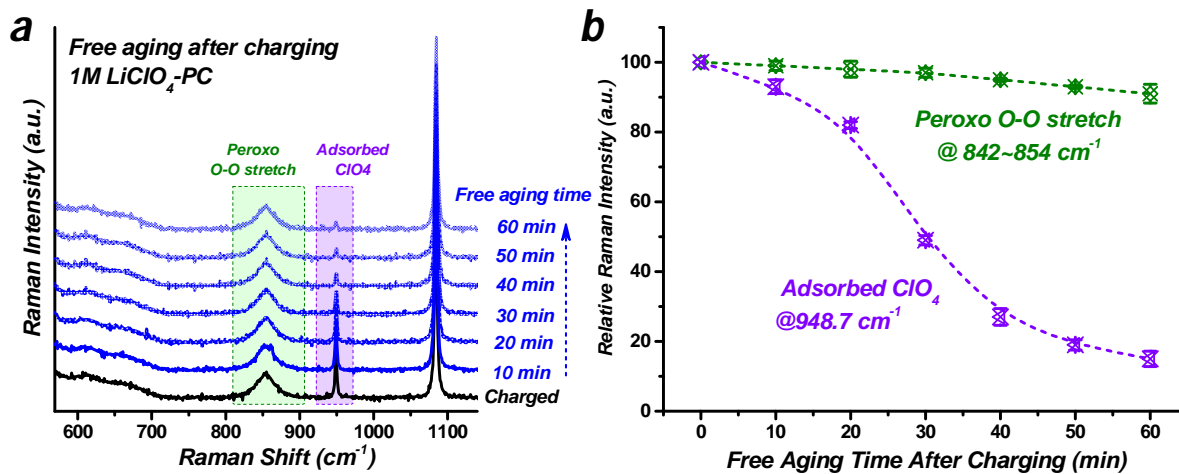


Figure S7. Aging time test of O-O peak and ClO₄⁻ peak after charging. a) Changes of Raman intensity with aging time and b) relative Raman intensity with aging time.

The change of unique adsorbed ClO₄⁻ peak is a function of potential. There is no relationship between O-O peak and adsorbed ClO₄⁻ peak, which can be confirmed by aging test. As shown in **Figure S7**, we stopped the procedure and let the cell free at the end of charging process. The variation of Raman intensity of O-O peak and ClO₄⁻ peak are obvious in **Figure S7a** and more distinct in **Figure S7b**. The intensity of ClO₄⁻ peak decreases dramatically as a function of aging time, resulting from the essential reason-decrease of the potential. The intensity of O-O peak, however, basically remain unchanged with aging time.

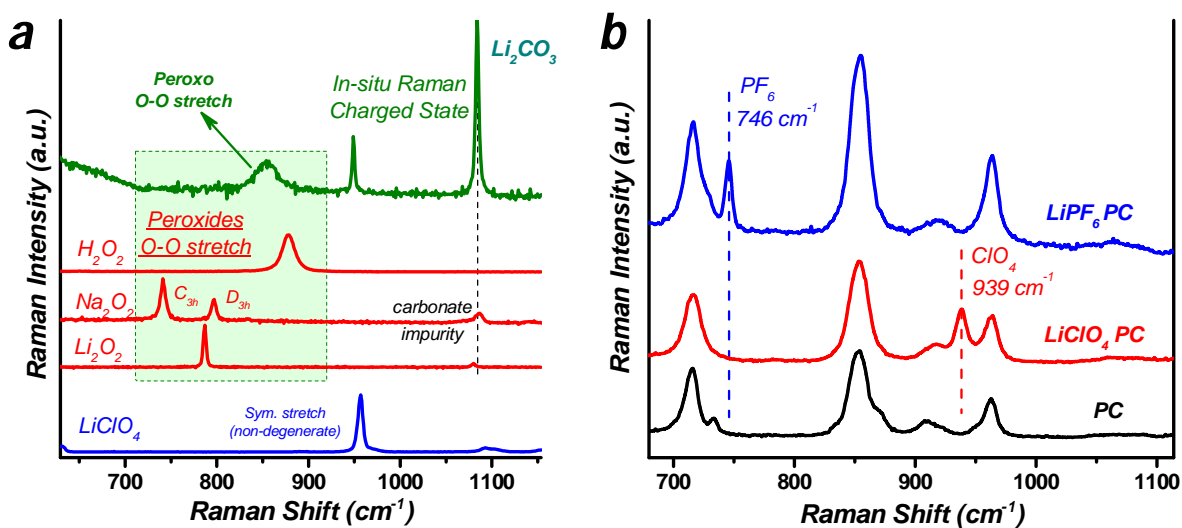


Figure S8. Raman peaks of standard materials of a) LiClO_4 , Li_2O_2 , Na_2O_2 , H_2O_2 , and charged state electrode and b) PC, electrolyte of 1M LiClO_4 in PC and electrolyte of 1M LiPF_6 in PC.

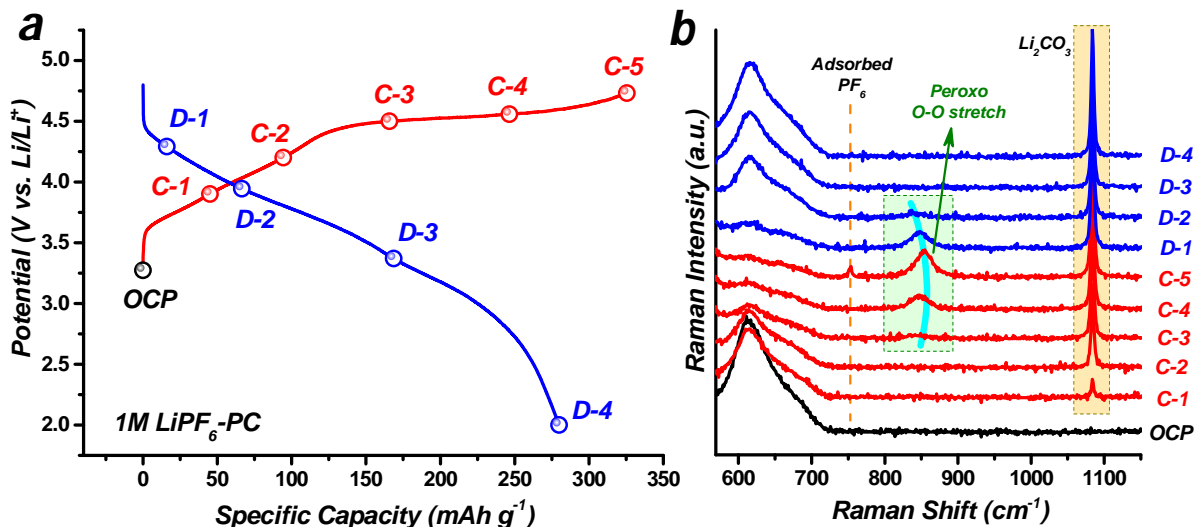


Figure S9. a) Typical charge-discharge profiles between 2.0 and 4.7 V with electrolyte of 1M LiPF₆ in PC at 10 mA g⁻¹ and b) in situ Raman spectra recorded during initial galvanostatic cycle.

The phenomenon of adsorbed ClO₄⁻ peak coupled with peroxide species in **Figure 3**, however, made a confusion because it seems ClO₄⁻ may be additional source for O-O dimers. We have confirmed that the adsorbed ClO₄⁻ peak is potential-dependent and has no relationship with O-O bonding. Furthermore, we did the similar experiment in LiPF₆ (1M in PC), as shown in **Figure S9**. A new peak (O-O) at ~ 850 cm⁻¹ emerges and increases during the 4.5 V-related charging plateau, and gradually disappears with the subsequent discharge process, similar to the phenomenon in LiClO₄-salt electrolyte. Another similar phenomenon is that a new peak at ~ 1080 cm⁻¹ emerges and increases during the charging process and without decrease even in discharging process, which can be assigned to Li₂CO₃. Moreover, the adsorbed PF₆⁻ peak appears until the end of charging process, which is also potential-dependent.

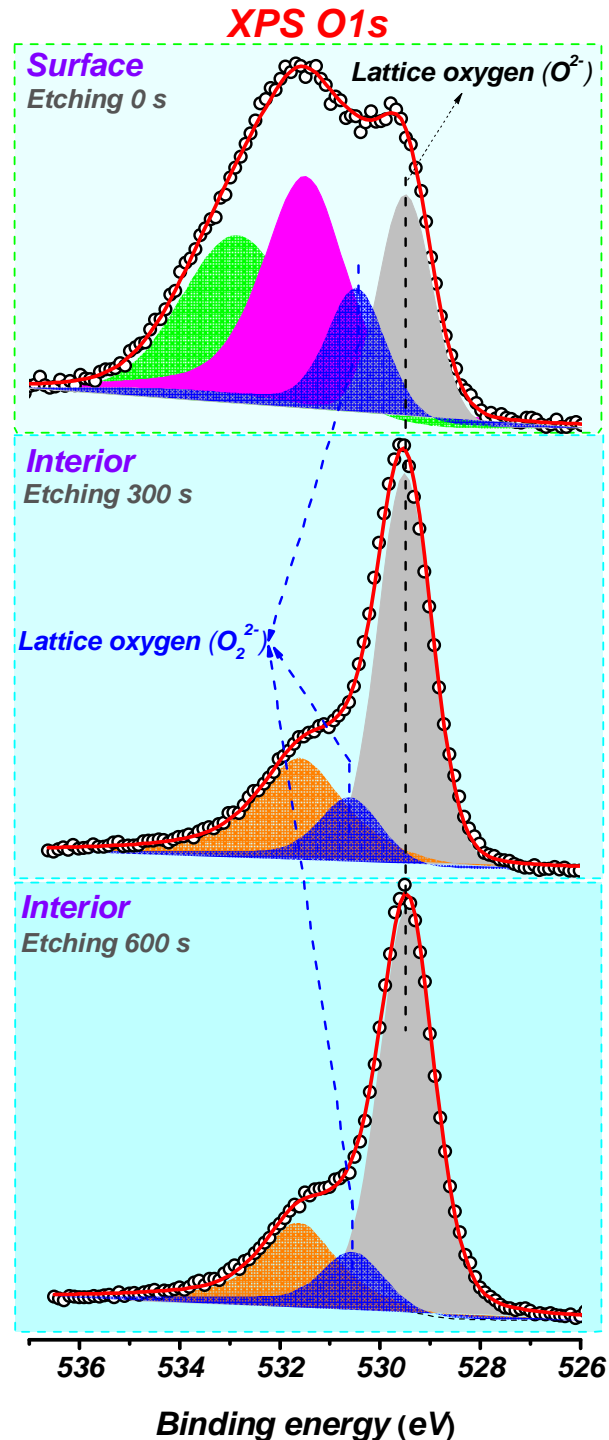


Figure S10: Oxygen 1s XPS spectra of the charged $\text{Li}_{1.2}\text{Ni}_{0.2}\text{Mn}_{0.6}\text{O}_2$ electrode at 4.7 V, which were collected in the surface, after Ar^+ etching 300 s and 600 s. The grey, blue, green, and pink areas represent the lattice oxygen (O^{2-}), lattice oxygen (O_2^{2-}), surface deposited species and electrolyte oxidation, respectively. The brown area may be caused by the oxygen deficiencies.

To understand the formation of O-O dimers in the bulk or in the surface, depth analysis was employed by the X-ray photoelectron spectroscopy (XPS). XPS spectra were obtained from the

surface of the charged electrode at 4.7 V and that after different times of Ar⁺-sputtering. Before etching by argon sputtering, peaks were observed at ~ 529.5 eV, 530.5 eV, 531.5 eV, and 532.8 eV which are assigned to lattice oxygen (O²⁻), lattice oxygen (O₂²⁻), surface deposited species and electrolyte oxidation, respectivily. The peaks and their positions are consistent well with Tarascon and co-authours' works.^[9] After argon sputtering, the peak assigned to electrolyte oxidation disappears. The spectrum after etching 300 s is as same as that after etching 600 s, meaning the internal structure was obtained after sputtering 300 s. Obviously, the peak located at 530.5 eV (bule area) can be clearly seen after sputtering, which is assigned to peroxy oxygen dimers (the brown area may be caused by the oxygen deficiencies^[10]). Herein, the peroxy oxygen dimers exist both in surface and in internal. Note that, the composition of the electrode may change after sputtering, however, the result can be reliable after some concessions we made in etching time and pattern quality.^[11]

DFT calculation model:

Lithium honeycomb ordering is common in many lithium-excess compounds, corresponding to the additional superlattice peaks in XRD pattern. However, the honeycomb structure is short-range order because of the non-uniform distribution of the cations (Li, Ni, Mn) in transition metal layers.^[12] It means that there exist mixed ordering types such as honeycomb-type and straight-type in transition metal layers.^[12, 13] Here, we present the detailed reasons why we chose the straight-type model for first principle calculation, after considering the several configurations in transition-metal layers.

In our calculations, the honeycomb type ordering of excess lithium atoms was studied. Considering the balance between computing workloads and the accuracy of calculation model, a lithium honeycomb type ordering structure with the composition of $\text{Li}_{1.22}\text{Ni}_{0.22}\text{Mn}_{0.56}\text{O}_2$ is built, as shown in Figure S11. Although the composition of $\text{Li}_{1.22}\text{Ni}_{0.22}\text{Mn}_{0.56}\text{O}_2$ is slightly different from our experimental $\text{Li}_{1.2}\text{Ni}_{0.2}\text{Mn}_{0.6}\text{O}_2$, it can well represent the local honeycomb ordering of lithium atoms in $\text{Li}_{1.2}\text{Ni}_{0.2}\text{Mn}_{0.6}\text{O}_2$. Thus, we investigated the peroxy bond formation in the fully delithiated $\text{Li}_{1.22}\text{Ni}_{0.22}\text{Mn}_{0.56}\text{O}_2$ compound, whose honeycomb ordered Li atom in transition metal layer are fully extracted to represent the charging final structure. The corresponding energy barrier of the peroxy bond formation in it is depicted in Figure S12. It can be seen that forming a peroxy bond with the O-O bond length less than 1.46 Å (a typical value of peroxy bond)^[14] in this lithium honeycomb type structure is endothermic, more than 1 eV ~96 KJ/mol, and needs to overcome a very large energy barrier of 1.44 eV. Such high energy barriers of peroxy bond formation also can be found in Li_2MnO_3 compounds, 0.6-1 eV.^[14] Generally, the thermal vibration energy of an atom is KT , ~0.026 eV at 300K, which is far less than the energy barrier for the peroxy bond formation, so the possibility of forming peroxy bonds in the lithium-excess compounds with

the local lithium honeycomb type structure in $\text{Li}_{1.2}\text{Ni}_{0.2}\text{Mn}_{0.6}\text{O}_2$ during the charging and discharging process at room environment is extremely low.

We calculated the relative energy of some other $\text{Li}_{1.2}\text{Ni}_{0.2}\text{Mn}_{0.6}\text{O}_2$ structures with different lithium atom orderings in transition metal layer, as shown in Figure S13. Refer to the case 1 with dispersive lithium atom orderings, the relative energy of case 5 structure with local lithium straight-type tripolymers is 35.45 meV/atom, slightly more than the room temperature atom thermal vibration energy ~26 meV/atom, but far less than the high temperature atom thermal vibration energy ~101.67 meV/atom at the synthesizing temperature of 900 °C. Therefore, the lithium straight-type tripolymers in some local areas of our experimental case are highly possible, and they are also observed in some other lithium-excess compounds, such as $\text{Li}_{1.15}\text{Ni}_{0.47}\text{Sb}_{0.38}\text{O}_2$.^[13]

In addition, we have investigated the peroxy bond formation in these $\text{Li}_{1.2}\text{Ni}_{0.2}\text{Mn}_{0.6}\text{O}_2$ structures in Figure S13. Similarly, forming peroxy bonds in these structures are difficult with larger energy barriers compared to straight-type tripolymer structure. While the local lithium straight-type tripolymers model (Figure S14) is beneficial for the formation of peroxy bonds without energy barrier, which is a spontaneous exothermic process. Therefore, the local lithium straight-type tripolymers model in DFT calculations can explain the formation and evolution of peroxy bonds during the charging and discharging process of our experiment.

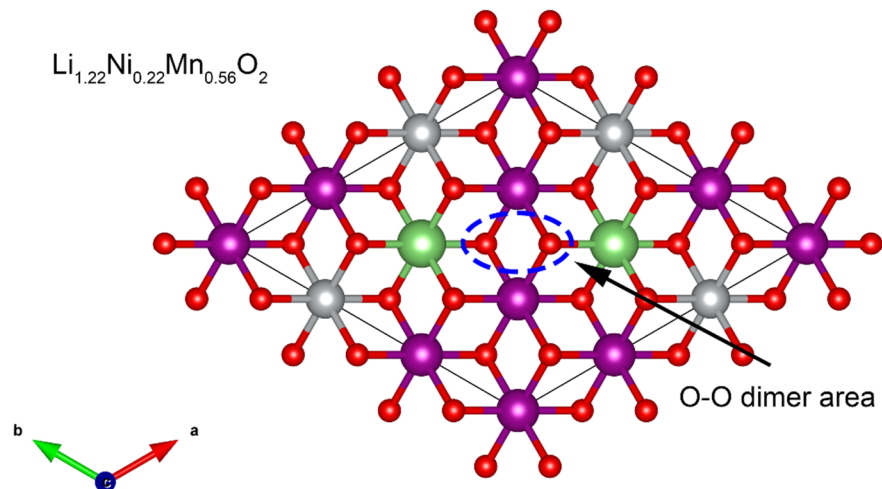


Figure S11. Honeycomb ordering of Li atoms in the transition metal layer of lithium-excess $\text{Li}_{1.22}\text{Ni}_{0.22}\text{Mn}_{0.56}\text{O}_2$ compound. The white, purple, green and red spheres represent Li, Mn, Ni and O atoms, respectively.

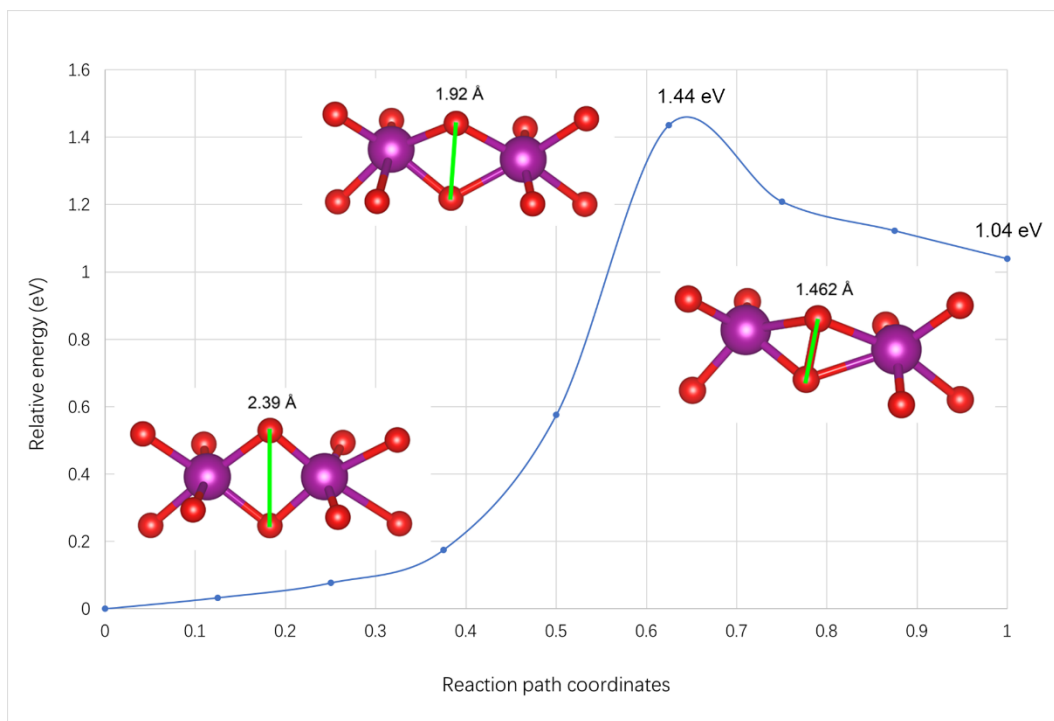


Figure S12. Energy barrier (eV) of the peroxy bond formation in fully delithiated $\text{Li}_{1.22}\text{Ni}_{0.22}\text{Mn}_{0.56}\text{O}_2$ compound with honeycomb orderings of Li atoms at the end of charging (Insets are the local structures for peroxy bond formation, including initial structure, transition state structure and final structure).

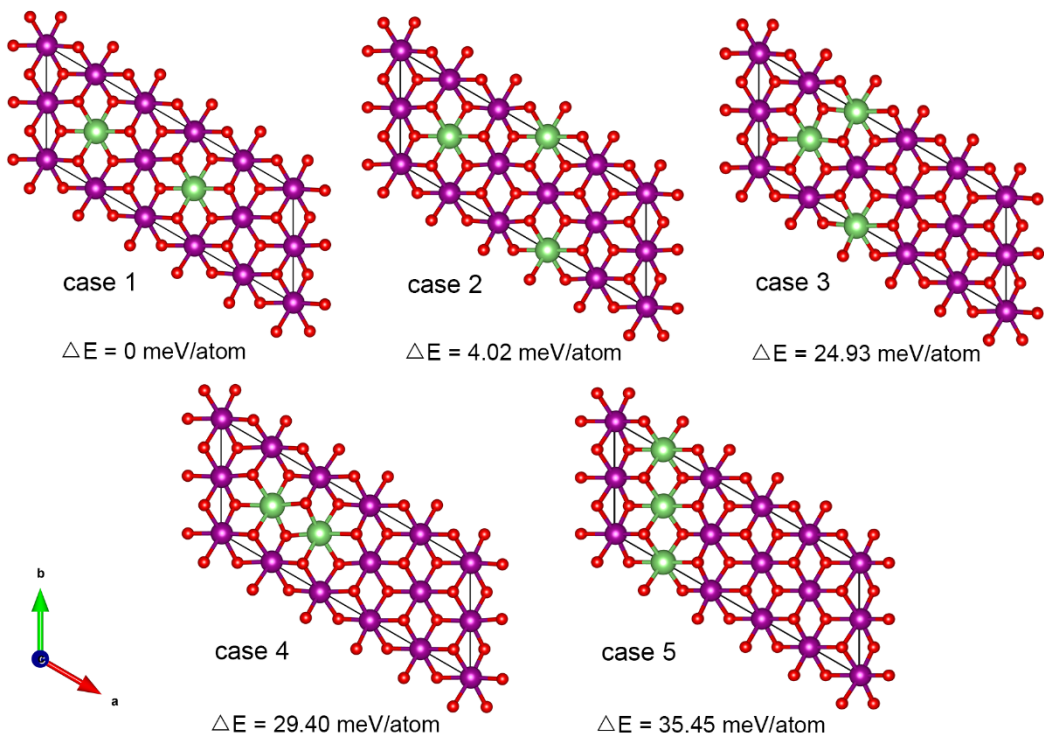


Figure S13. The relative energy (in meV/atom, and referred to case 1) of $\text{Li}_{1.2}\text{Ni}_{0.2}\text{Mn}_{0.6}\text{O}_2$ compounds with different lithium atom orderings in the transition metal layer.

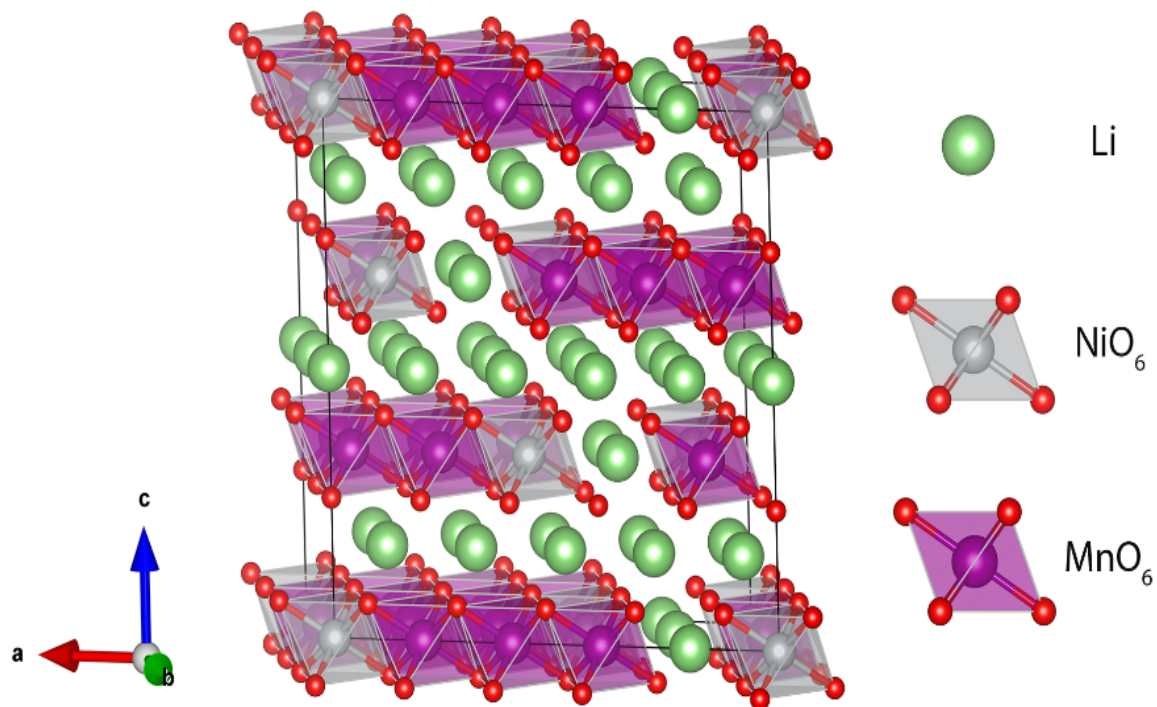


Figure S14. The optimized crystal structure of $\text{Li}_{1.2}\text{Ni}_{0.2}\text{Mn}_{0.6}\text{O}_2$. The green, silver, purple and red spheres represent Li, Ni, Mn and O atoms, respectively.

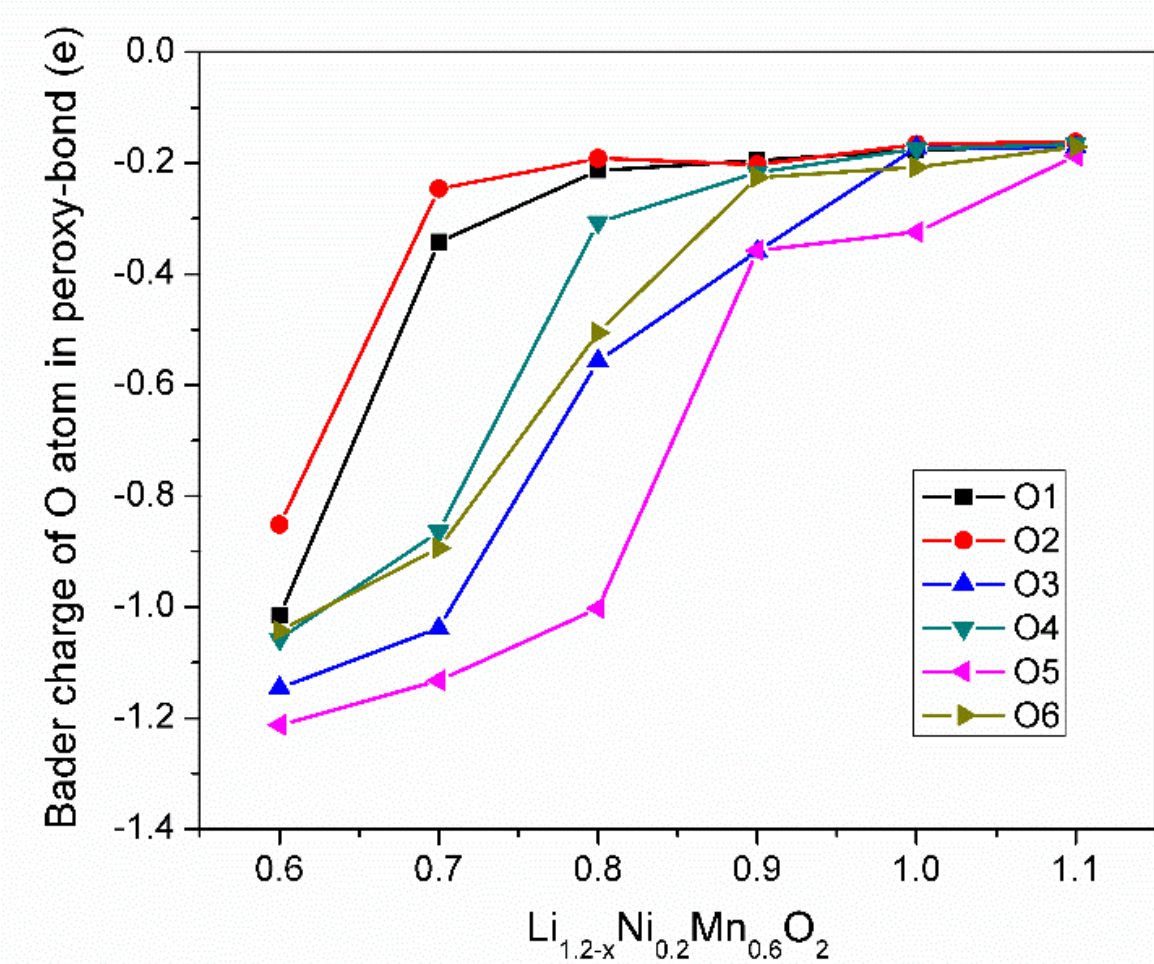


Figure S15. O atomic Bader charge (e) of the peroxy O-O bonds of the $\text{Li}_{1.2-x}\text{Ni}_{0.2}\text{Mn}_{0.6}\text{O}_2$ systems ($x = 0.6, 0.7, 0.8, 0.9, 1.0$ and 1.1) during the charging and discharging processes

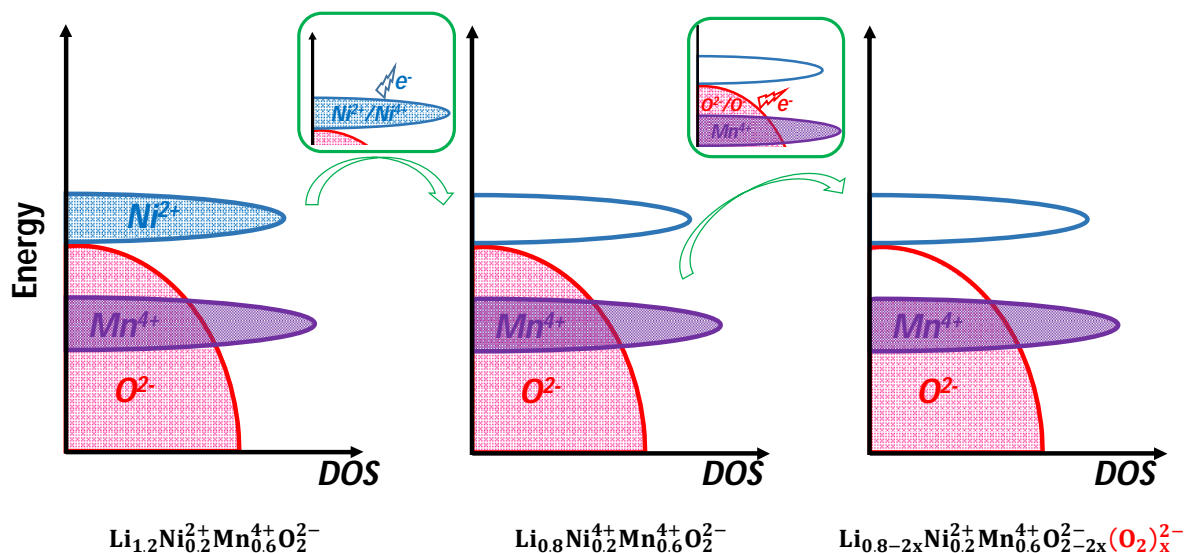


Figure S16. Schematic representation of the density of states (DOS) of $\text{Li}_{1.2}\text{Ni}_{0.2}\text{Mn}_{0.6}\text{O}_2$ during charge process.

Table S17. Crystallographic parameters obtained from the Rietveld refinement for the Li_2MnO_3 (C2/m) phase of $\text{Li}_{1.2}\text{Ni}_{0.2}\text{Mn}_{0.6}\text{O}_2$.

Li_2MO_3 (C2/m) $R_{wp}=0.023$ $R_p=0.017$						
$a = 4.959\text{\AA}$, $b = 8.284\text{\AA}$ $c = 5.037\text{\AA}$ $\beta = 109.07^\circ$						
Atom	site	x	y	z	Occ.theo	Occ.refined
Mn	4g	0	0.165	0	0.9	0.9
Ni	4g	0	0.165	0	0.1	0.0948
Li	4g	0	0.165	0	0	0.0052
Ni	2c	0	0	0.5	0	0.0020
Li	2c	0	0	0.5	1	0.9980
Ni	4h	0	0.66	0.5	0	0.0036
Li	4h	0	0.66	0.5	1	0.9964
Li	2b	0	0.5	0	0.6	0.5988
Ni	2b	0	0.5	0	0.4	0.4012
O	4i	0.178	0	0.208	1	1
O	8j	0.253	0.320	0.231	1	1

Reference:

- [1] J. Ye, Y. X. Li, L. Zhang, X. P. Zhang, M. Han, P. He, H. S. Zhou, *ACS Appl. Mater. Interfaces* **2016**, *8*, 208.
- [2] Y. Qiao, S. Wu, J. Yi, Y. Sun, S. Guo, S. Yang, P. He, H. Zhou, *Angew. Chem. Int. Ed.* **2017**, *56*, 4960.
- [3] J. F. Li, Y. F. Huang, Y. Ding, Z. L. Yang, S. B. Li, X. S. Zhou, F. R. Fan, W. Zhang, Z. Y. Zhou, Y. WuDe, B. Ren, Z. L. Wang, Z. Q. Tian, *Nature* **2010**, *464*, 392
- [4] P. E. Blöchl, *Phys. Rev. B* **1994**, *50*, 17953.
- [5] W. Kohn, L. J. Sham, *Phys. Rev.* **1965**, *140*, A1133.
- [6] J. P. Perdew, K. Burke, M. Ernzerhof, *Phys. Rev. Lett.* **1996**, *77*, 3865.
- [7] H. J. Monkhorst, J. D. Pack, *Phys. Rev. B* **1976**, *13*, 5188.
- [8] a) N. Yabuuchi, K. Yoshii, S.-T. Myung, I. Nakai, S. Komaba, *J. Am. Chem. Soc.* **2011**, *133*, 4404; b) S. Hy, F. Felix, J. Rick, W. N. Su, B. J. Hwang, *J. Am. Chem. Soc.* **2014**, *136*, 999.
- [9] a) E. McCalla, A. M. Abakumov, M. Saubanere, D. Foix, E. J. Berg, G. Rousse, M. L. Doublet, D. Gonbeau, P. Novak, G. Van Tendeloo, R. Dominko, J. M. Tarascon, *Science* **2015**, *350*, 1516; b) M. Sathiya, G. Rousse, K. Ramesha, C. P. Laisa, H. Vezin, M. T. Sougrati, M. L. Doublet, D. Foix, D. Gonbeau, W. Walker, A. S. Prakash, M. Ben Hassine, L. Dupont, J. M. Tarascon, *Nat. Mater.* **2013**, *12*, 827; c) M. Sathiya, A. M. Abakumov, D. Foix, G. Rousse, K. Ramesha, M. Saubanere, M. L. Doublet, H. Vezin, C. P. Laisa, A. S. Prakash, D. Gonbeau, G. VanTendeloo, J. M. Tarascon, *Nat. Mater.* **2015**, *14*, 230; d) P. E. Pearce, A. J. Perez, G. Rousse, M. Saubanère, D. Batuk, D. Foix, E. McCalla, A. M. Abakumov, G. Van Tendeloo, M.-L. Doublet, J.-M. Tarascon, *Nat. Mater.* **2017**, *16*, 580.

- [10] a) J.-C. Dupin, D. Gonbeau, P. Vinatier, A. Levasseur, *Phys. Chem. Chem. Phys.* **2000**, *2*, 1319; b) L. Dahéron, R. Dedryvere, H. Martinez, M. Ménétrier, C. Denage, C. Delmas, D. Gonbeau, *Chem. Mater.* **2007**, *20*, 583.
- [11] D. Aurbach, I. Weissman, A. Schechter, H. Cohen, *Langmuir* **1996**, *12*, 3991.
- [12] J. S. Kim, C. S. Johnson, J. T. Vaughey, M. M. Thackeray, S. A. Hackney, *Chem. Mater.* **2004**, *16*, 1996.
- [13] N. Twu, X. Li, A. Urban, M. Balasubramanian, J. Lee, L. Liu, G. Ceder, *Nano Lett.* **2014**, *15*, 596.
- [14] H. R. Chen, M. S. Islam, *Chem. Mater.* **2016**, *28*, 6656.